

pubs.acs.org/cm Article

Short Aromatic Diammonium Ions Modulate Distortions in 2D Lead Bromide Perovskites for Tunable White-Light Emission

Ping Fu, Michael A. Quintero, Claire Welton, Xiaotong Li, Bruno Cucco, Michael C. De Siena, Jacky Even, George Volonakis, Mikaël Kepenekian, Runze Liu, Craig C. Laing, Vladislav Klepov, Yukun Liu, Vinayak P. Dravid, G. N. Manjunatha Reddy, Can Li, and Mercouri G. Kanatzidis*



Cite This: Chem. Mater. 2022, 34, 9685-9698



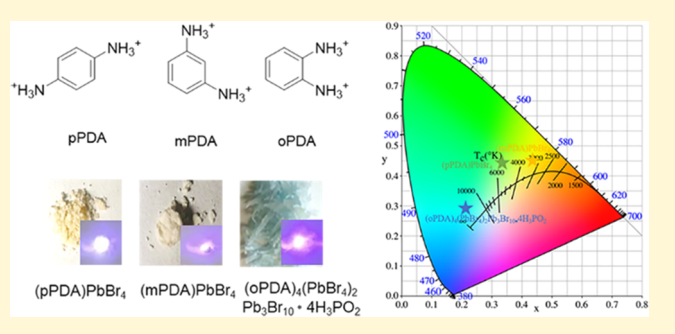
ACCESS

Metrics & More

Article Recommendations

s Supporting Information

ABSTRACT: White-light broadband emission in the visible range from the low-dimensional halide perovskites is commonly attributed to structural distortions in lead bromide octahedra. In this paper, we report Dion—Jacobson-phase two-dimensional (2D) lead bromide perovskites based on short aromatic diammonium cations, p-phenylene diammonium (pPDA), m-phenylene diammonium (mPDA), and two 1D compounds templated by ophenylene diammonium (oPDA). All of the compounds exhibit white-light emission. Single-crystal X-ray diffraction analysis reveals that the distortion of the Pb octahedra is influenced by the stereochemistry of the cations and their interactions with the



perovskite layers. Solid-state ¹H and ²⁰⁷Pb NMR spectroscopy analysis further confirms this trend, whereby different ¹H and ²⁰⁷Pb chemical shifts are observed for the pPDA and mPDA spacer cations, indicating different hydrogen-bonding interactions and octahedral distortions. Owing to the octahedral distortion, 2D (mPDA)PbBr₄ compounds exhibit broader white-light emission than 2D (pPDA)PbBr₄. Density functional theory calculations suggest that (pPDA)PbBr₄ and (mPDA)PbBr₄ are direct-band-gap semiconductors, and they exhibit larger electronic band gaps and effective masses than the Ruddlesden–Popper-phase (BA)₂PbBr₄. Among the films of these compounds, 2D (mPDA)PbBr₄ shows the best stability, which is attributed to stronger hydrogen-bonding interactions in the material.

1. INTRODUCTION

Organic-inorganic hybrid perovskites are promising candidates for optoelectronic devices, such as solar cells 1-4 and light-emitting diodes (LEDs), 5,6 owing to their unique optical properties and high tunability. The prototypical organicinorganic hybrid perovskites exhibit the general formula AMX₃ (A = methylammonium (MA, $CH_3NH_3^+$), formamidinium $(FA, CH_3(NH_2)_2^+)$, or Cs^+ ; $M = Sn^{2+}$ or Pb^{2+} ; $X = Cl^-$, Br^- , or I⁻). Inorganic ions form a framework with corner-sharing octahedral [MX₆]⁴⁻ units, and the small A-site cations occupy cuboctahedral voids within the framework and counterbalance the charge of the [MX₆]⁴⁻ extended anion. When larger spacer cations are incorporated, the structure tends to split along different crystallographic planes, typically (100), (110), and (111) planes. The resulting two-dimensional (2D) perovskites have different band structures compared to their three-dimensional (3D) counterparts and exhibit larger structural distortions within their metal halide octahedra.8 Among them, Dion-Jacobson (DJ)-phase 2D perovskites, consisting of short diamine spacer cations between the perovskite halide slabs, represent a special class in which the slabs can come very close together and form nonbonding X···X contacts. 11,12 This gives rise to unique phenomena, such as

enhancing the electronic coupling between perovskite layers across the organic spacer and enhancing the charge transport. ¹³ Further slicing of 2D perovskites results in metal halide wires and the formation of individual octahedra, one-dimensional (1D) and zero-dimensional (0D) structures. ¹⁴

Since 2D lead bromide perovskites exhibit broadband white-light emission, ¹⁵ several other 2D perovskites, ^{16–18} and even some lower-dimensional metal halide hybrids, such as 1D^{19–21} and 0D perovskitoids^{22,23} have also demonstrated white-light emission at room temperature. Because different spacer cations can impose various structural distortions, it is essential to study their effects on the nature of light emission properties of these materials. Moreover, identifying novel spacer cations will help further elucidate the relationship between cation choice, structural distortions, and light emission. Compared to the flexible aliphatic alkylammonium cations, mainly used for

Received: August 11, 2022 Revised: September 30, 2022 Published: October 20, 2022





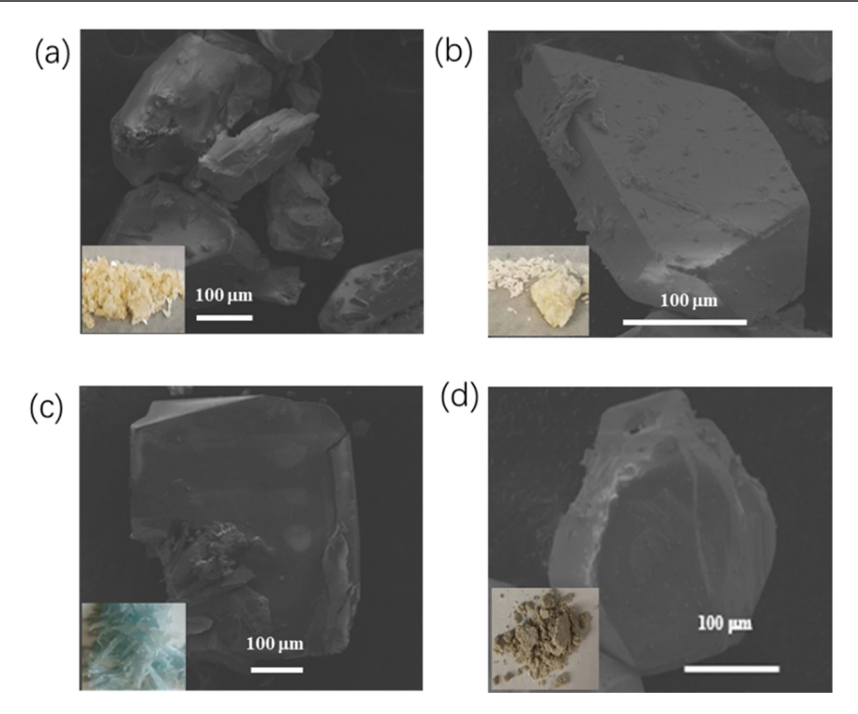


Figure 1. SEM images for (a) $(pPDA)PbBr_4$, (b) $(mPDA)PbBr_4$, (c) $(oPDA)_4(PbBr_4)_2Pb_3Br_{10}\cdot 4$ H_3PO_2 , and (d) $(oPDA)_2Pb_3Br_{10}$. Scale bar is 100 μ m.

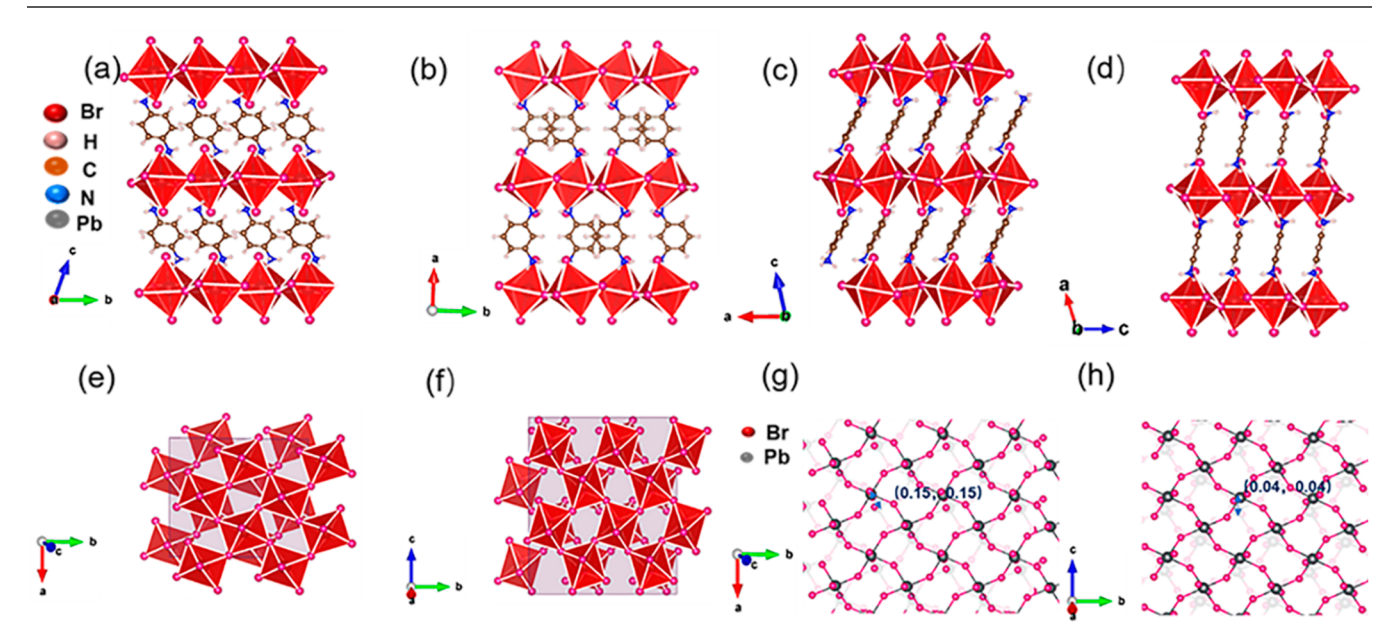


Figure 2. Different views of the 2D structures (a, c, e, g) (pPDA)PbBr₄ and (b, d, f, h) (mPDA)PbBr₄, respectively. The offset of the adjacent inorganic layer is estimated by the shift distance of Pb/2 × length (Pb-Br).

broad white-light emission,^{24–26} the rigid aromatic cations offer several unique attributes to 2D perovskites. These include greater delocalization of the positive charge on the aromatic ring, shorter interlayer spacing, more hydrogen bonding between cations and anions, higher dielectric constants, and lower exciton binding energies.^{27,28} Therefore, incorporating rigid aromatic cations into perovskite structures can result in various distortions and expansion for different types of broademission activity.

In this study, we employed three rigid isomers, viz., aromatic para-phenylene diammonium (pPDA), meta-phenylene diammonium (mPDA), and ortho-phenylene diammonium

(oPDA) dications to template 2D lead bromide perovskites. We observed a nontrivial influence of each isomer on the crystal structure and physical properties. The first two cations are stabilized within the 2D perovskite motif, whereas oPDA leads to new 1D structural arrangements. The detailed crystallographic structures of 2D (pPDA)PbBr₄, 2D (mPDA)-PbBr₄, 1D (oPDA)₄(PbBr₄)₂Pb₃Br₁₀·4H₃PO₂, and 1D (oPDA)₂Pb₃Br₁₀ perovskites reveal the precise cation—anion interactions in these emissive materials. In addition, the local structures and packing interactions at the organic—inorganic interfaces were analyzed using ¹H and ²⁰⁷Pb solid-state NMR spectra. All of the compounds exhibit white-light emission, the

Table 1. Crystal and Refinement Data for 2D (pPDA)PbBr₄, 2D (mPDA)PbBr₄, 1D (oPDA)₄(PbBr₄)₂Pb₃Br₁₀·4 H₃PO₂, and 1D (oPDA)₂Pb₃Br₁₀ at 293 K, Respectively^a

empirical formula	(pPDA)PbBr ₄	$(mPDA)PbBr_4$	$(\text{oPDA})_4(\text{PbBr}_4)_2 \text{ Pb}_3\text{Br}_{10}\cdot 4\text{H}_3\text{PO}_2$	$(oPDA)_2Pb_3Br_{10}$			
formula weight	636.99	636.99	3237.2	1640.99			
crystal system	triclinic	monoclinic	triclinic	triclinic			
space group	$P\overline{1}$	C2/c	$P\overline{1}$	$P\overline{1}$			
unit cell dimensions	a = 7.4473(15) Å,	a = 21.776(4) Å,	a = 7.7604(16) Å,	a = 7.5730(15) Å,			
	$\alpha = 70.53(3)^{\circ}$	$\alpha = 90^{\circ}$	$\alpha = 89.87(3)^{\circ}$	$\alpha = 104.45(3)^{\circ}$			
	b = 8.7255(17) Å,	b = 8.8113(18) Å,	b = 14.578(3) Å,	b = 10.323(2) Å,			
	$\beta = 78.47(3)^{\circ}$	$\beta = 107.16(3)^{\circ}$	$\beta = 77.79(3)^{\circ}$	$\beta = 96.43(3)^{\circ}$			
	c = 11.036(2) Å,	c = 7.3950(15) Å,	c = 16.021(3) Å,	c = 11.235(2) Å,			
	$\gamma = 89.40(3)^{\circ}$	$\gamma = 90^{\circ}$	$\gamma = 84.54(3)^{\circ}$	$\gamma = 110.67(3)^{\circ}$			
volume	661.2(3) Å ³	1355.7(5) Å ³	$1763.1(7) \text{ Å}^3$	776.2(3) $Å^3$			
Z	2	4	1	1			
density (calculated)	3.199 g/cm^3	3.121 g/cm^3	2.983 g/cm^3	3.511 g/cm^3			
index ranges	-9 < = h < = 9,	-28 < = h < = 27,	-9 < = h < = 7,	-9 < = h < = 12,			
	-11 < = k < = 10,	-11 < = k < = 11,	-17 < = k < = 17,	-16 < = k < = 16,			
	-14 < = 1 < = 14	-9 < = 1 < = 9	-19 < = 1 < = 19	-17 < = 1 < = 18			
reflections collected	10,586	5664	14,009	12,512			
independent reflections	$3027 [R_{int} = 0.0864]$	$1556[R_{\rm int} = 0.1141]$	$6180 [R_{int} = 0.0529]$	$6702[R_{\text{int}}=0.0471]$			
completeness to θ = 25.000°	99.7%	99.5%	99.4%	99.2%			
data/restraints/parameters	3027/0/124	1556/0/65	6180/0/313	6702/0/135			
goodness-of-fit	1.172	1.122	1.024	1.035			
final R indices $[I > 2\sigma(I)]$	$R_{\rm obs} = 0.0826,$	$R_{\rm obs} = 0.0507,$	$R_{\rm obs} = 0.0525,$	$R_{\rm obs} = 0.0499$, w $R_{\rm obs} = 0.1002$			
	$wR_{\rm obs} = 0.2092$	$wR_{\rm obs} = 0.1258$	$wR_{\rm obs} = 0.1357$				
R indices [all data]	$R_{\rm all} = 0.1094,$	$R_{\rm all} = 0.0572,$	$R_{\rm all} = 0.0652,$	$R_{\text{all}} = 0.1150, \text{ w}R_{\text{all}} = 0.1364$			
	$wR_{\rm all} = 0.2600$	$wR_{\rm all} = 0.1322$	$wR_{\rm all} = 0.1454$				
largest diff. peak and hole	4.775 and -4.662 e·Å ⁻³	$2.669 \text{ and } -2.365 \text{ e} \cdot \text{Å}^{-3}$	1.963 and -2.542 e-Å^{-3}	$2.048 \text{ and } -3.547 \text{ e} \cdot \text{Å}^{-3}$			
${}^{a}R = \sum F_{o} - F_{c} / \sum F_{o} , \ wR = \{\sum [w(F_{o} ^{2} - F_{c} ^{2})^{2}] / \sum [w(F_{o} ^{4})]\}^{1/2}.$							

wavelength and width of which are linked to the level of distortion in the inorganic framework. Density functional theory calculations suggest that (pPDA)PbBr₄ and (mPDA)PbBr₄ are direct-band-gap semiconductors, and they exhibit larger electronic band gaps and effective masses than those of the corresponding Ruddlesden—Popper phases (BA)₂PbBr₄ (BA = butylammonium). Films of these materials were prepared successfully from N_1N_1 -dimethylformamide (DMF) solvent. The film stability test shows that the stronger hydrogen-bonding interactions in the (mPDA)PbBr₄ contribute to better thermal and light stability.

2. RESULTS AND DISCUSSION

2.1. Single-Crystal Growth and Structures. The new compounds were synthesized in hydrobromic acid (HBr) and hypophosphorous acid (H_3PO_2) medium using a step-cooling method as previously reported. By tuning the stoichiometric ratios of lead oxide and spacer cations according to the chemical formula of (xPDA)PbBr₄, 2D (pPDA)PbBr₄ and (mPDA)PbBr₄ perovskite structures are obtained in a targeted manner. The detailed procedure for the single-crystal growth is described in the Experimental Section. It is worth noting that the pPDA cation behaves differently in bromide and iodide chemistry. Previous work demonstrates that in the case of iodide, the pPDA cation forms a hydrated 1D perovskite structure (pPDA)PbI₄·2H₂O. In the present case of bromides, we have the first example of 2D pPDAPbBr₄ perovskite structure (n = 1) with this cation.

The oPDA cation also behaves differently in the bromide system, which does not provide any evidence for the presence of perovskite "2D (oPDA)PbBr₄". The oPDA cations give the 1D (oPDA)₄(PbBr₄)₂Pb₃Br₁₀·4H₃PO₂ halide when H₃PO₂ is

added to the reaction, and the 1D (oPDA)₂Pb₃Br₁₀ structure when the reaction is carried out without H₃PO₂. The morphology and color of 2D (pPDA)PbBr₄, 2D (mPDA)-PbBr₄, 1D (oPDA)₄(PbBr₄)₂Pb₃Br₁₀·4H₃PO₂, and 1D (oPDA)₂Pb₃Br₁₀ are shown in Figure 1a–d. The successful synthesis of the desired materials in their pure form is further confirmed by powder X-ray diffraction (XRD) analysis, as shown in Figure S1. The observed patterns match the calculated values well.

The precise crystal structures are determined using singlecrystal XRD, and they are shown in Figure 2a-h. The selected crystallographic data and structural refinements are listed in Table 1. The compounds are refined in the centrosymmetric triclinic space group (P1) for 2D (pPDA)PbBr₄ and in the monoclinic space group (C2/c) for 2D (mPDA)PbBr₄. The octahedra in (pPDA)PbBr₄ and (mPDA)PbBr₄ form "cornersharing" 2D perovskite structures. The adjacent inorganic layer with respect to the nearest metal-metal distance for the 2D (pPDA)PbBr₄ and (mPDA)PbBr₄ are slightly offset, with a layer shift factor of (0.15, 0.15) and (0.04, 0.04), respectively, and they formally belong to the Dion–Jacobson (DJ) family (n = 1 members). $^{11,31-33}$ The adjacent [PbBr₄]²⁻ slabs are close but do not interact. For comparison, the standard van der Waals distance between the two bromine atoms is 3.7 Å. Specifically, the closest interlayer Br...Br distances are nonbonding at 4.43 and 4.60 Å for 2D (pPDA)PbBr₄ and 2D (mPDA)PbBr₄, respectively.

In the ideal tetragonal structure of the n = 1 members, the four nearest metal atoms in a plane form a square, and the octahedra are untitled (e.g., the Pb-Br-Pb angle is 180°), but for the tilted structures, as in the present cases, two opposite edges of the square are "pulled-in" and the other two are

Table 2. Bond Length Distortion, Bond Angle Variance, Optical Band Gaps Evaluated from the Onset of the Absorption Spectra, Energy at Maximum PL, Full Width at Half-Maximum of PL, and Average Lifetimes of the Compounds Calculated Based on the 2D (pPDA)PbBr₄, 2D (mPDA)PbBr₄, and 1D (oPDA)₄(PbBr₄)₂Pb₃Br₁₀·4H₃PO₂, Respectively

	(pPDA)PbBr ₄	(mPDA)PbBr ₄	(oPDA) ₄ (PbBr ₄) ₂ Pb ₃ Br ₁₀ ·4 H ₃ PO ₂	(mPDA)PbI ₄
Pb-X-Pb minimum angle (X = Br, I) ($^{\circ}$)	140.59(7)	143.03(4)		143.2(3)
Pb-X-Pb maximum angle (X = Br, I) (°)	143.56(9)	143.03(4)		144.4(2)
Pb-X-Pb average angles $(X = Br, I)$ (°)	142.08(8)	143.03(4)		143.8(3)
Bond angle variance ^a	39.12	45.88	16.54	234.16
Bond length distortion ^a	0.008	0.010	0.026	0.005
absorption edge (eV)	3.01	3.00	3.44	2.21
PL emission center (eV)	2.30	2.08	2.58	2.43
PL FWHM (eV)	0.69	0.73	0.62	0.21
CIE x	0.34	0.44	0.21	
CIE y	0.44	0.46	0.29	
CCT	5450	3000	>10,000	

^aThe bond length distortion (Δd) is defined by $\Delta d = \left(\frac{1}{6}\right) \sum \left[\frac{\mathrm{Id_n} - d}{d}\right]$, where d is the average Pb-Br bond distance and d_n represents six individual bond distances in the PbBr₆ octahedron.

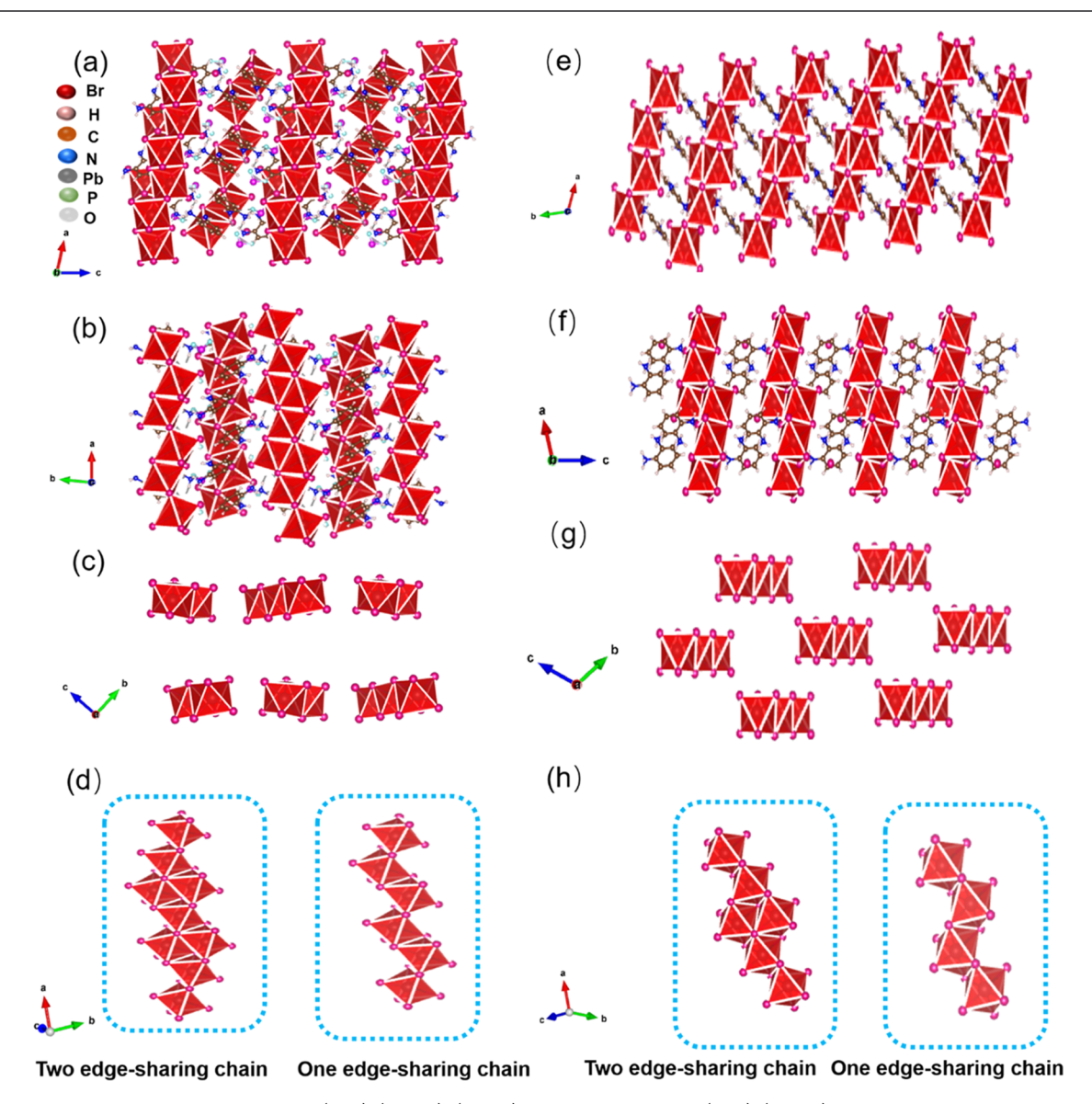


Figure 3. Different views of the 1D structures (a-c) $(oPDA)_4(PbBr_4)_2Pb_3Br_{10}4H_3PO_2$ and (e-g) $(oPDA)_2Pb_3Br_{10}$, respectively. Magnified images of one edge-sharing chain and two edge-sharing chains for $(oPDA)_4(PbBr_4)_2Pb_3Br_{10}$ \bullet 4H₃PO₂ (d) and $(oPDA)_2Pb_3Br_{10}$ (h), respectively.

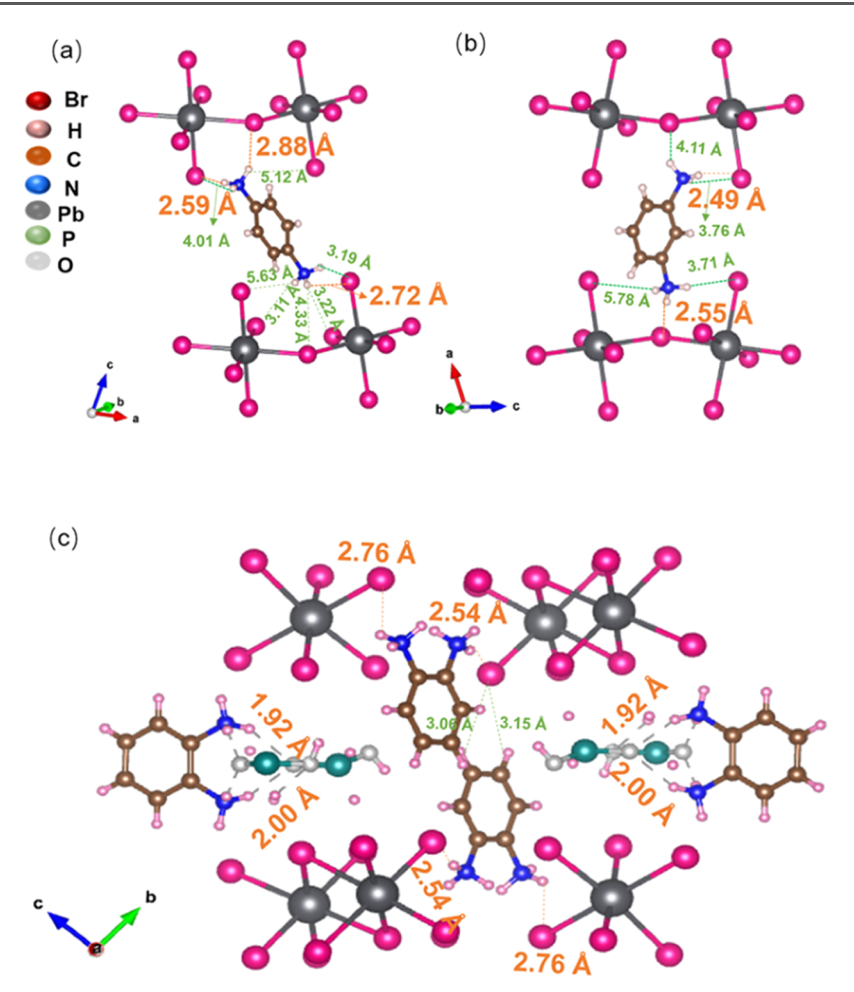


Figure 4. H-Br interactions for (a) (pPDA)PbBr₄, (b) (mPDA)PbBr₄, and (c) (oPDA)₄(PbBr₄)₂Pb₃Br₁₀·4 H₃PO₂.

"pushed-out". Specifically, the average Pb-Br-Pb angles were 142.08 and 143.03° for the 2D (pPDA)PbBr₄ and (mPDA)-PbBr₄, respectively, revealing considerable octahedra tilting. For comparison, (i) the typical RP phase (BA)₂PbBr₄ and (PEA)₂PbBr₄ (PEA: phenylethylamine), the average Pb-Br-Pb angles are 154.82 and 151.46°, respectively; ^{34,35} (ii) the new hybrid layered A_2PbBr_4 (A = 1,2,4-triazolium or acetamidinium) and AA'PbBr₄ (A = 1,2,4-triazolium and A' = imidazolium), templated by small disk-shaped amines, the average Pb-Br-Pb angles are 166.09, 164.4, and 176.98°, respectively. 18 It is evident that the average Pb-Br-Pb angles of the 2D (pPDA)PbBr₄ and (mPDA)PbBr₄ are the smallest. Thus, the short aromatic diammonium ions can modulate much more distorted octahedra in 2D lead bromide perovskites than in the RP and hybrid layered cases. The selected bond lengths and angles in the [PbBr₄] parts are listed in Table 2. The details of the structural distortion will be discussed later.

Additionally, both cations have phenyl groups, aromatic ring stacking $\pi-\pi$ interactions can occur if the distance between aromatic rings ranges from 3.3 to 3.8 Å. The distances between the stacked phenyl group for 2D (pPDA)PbBr₄ and 2D (mPDA)PbBr₄ are 3.81 and 3.63 Å, respectively. Both the cations in the 2D single-crystal structures have their benzene ring arranged in parallel (Figure 2c,d). The cations in (mPDA)PbBr₄ present stronger $\pi-\pi$ stacking interactions, while in (pPDA)PbBr₄ relatively weaker $\pi-\pi$ stacking interaction.

The oPDA cations template two kinds of "edge-sharing" 1D nonperovskite structures (both in the triclinic space group $P\overline{1}$), based on lead bromide with or without H_3PO_2 (Figure 3a–h). Notably, the 1D (oPDA)₄(PbBr₄)₂Pb₃Br₁₀·4H₃PO₂ single crystal with H_3PO_2 has a large cell volume of 1763.1(7) ų because of the inclusion of H_3PO_2 molecules, while a smaller volume of 776.2(3) ų (1763.1/2 = 881.5 ų normalized) is observed for 1D (oPDA)₂Pb₃Br₁₀ without H_3PO_2 molecules. The two 1D structures exhibit different unit cells, but both have two different types of zigzag 1D chains in their unit cell (Table 1). As shown in Figure 3d,h, one zigzag chain is connected by one edge-sharing octahedron and the other one is connected by two edge-sharing octahedra. These structures have rarely been found before and will be explained in detail below.

The short aromatic spacer cations mPDA and pPDA strongly influence the perovskite structure and properties. To understand the distortions in these structures, we calculated the mean distortion level in the octahedra of each compound. The bond length distortion, (Δd) is defined by $\Delta d = \left(\frac{1}{6}\right) \sum \left[\frac{\mathrm{Id}_n - d\mathrm{I}}{d}\right]$, where d is the average Pb-Br bond distance and d_n represents the six individual bond distances.^{37,38} The deformation of the octahedra can also be seen from the values of the bond angle variance (σ) calculated by the expression $\sigma^2 = \sum_1^{12} i(\theta_i - 90)^2/11$, where θ_i is the individual Br-Pb-Br bond angle.³⁹ The bond length

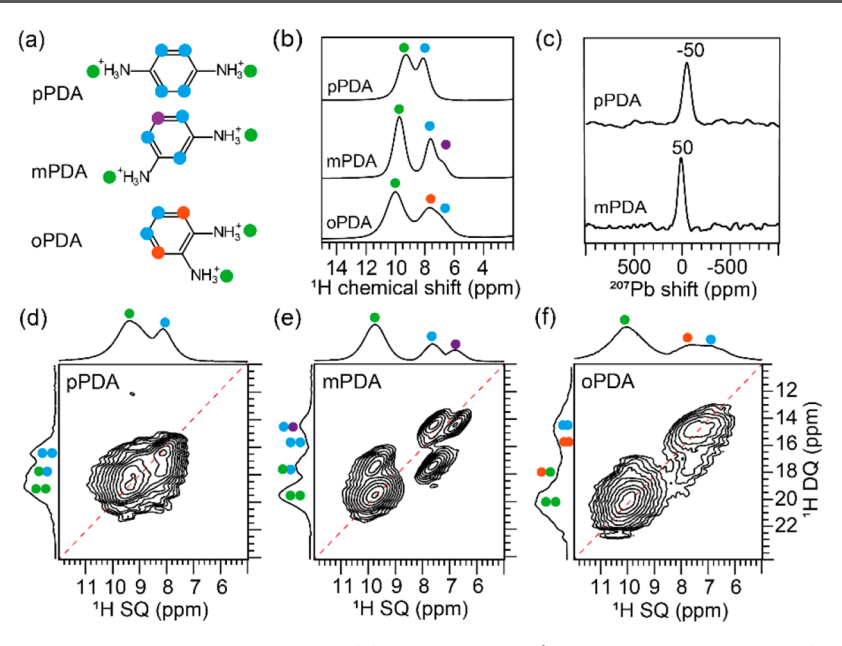


Figure 5. (a) Structures of p, m, and oPDA spacer cations. (b) Solid-state 1D ¹H MAS NMR spectra of (pPDA)PbBr₄, (mPDA)PbBr₄, (oPDA)₄(PbBr₄)₂Pb₃Br₁₀4H₃PO₂. (c) 1D ²⁰⁷Pb MAS NMR spectra of (pPDA)PbBr₄ and (mPDA)PbBr₄ perovskites. Solid-state 2D ¹H−¹H DQ-SQ correlation NMR spectra of (d) (pPDA)PbBr₄, (e) (mPDA)PbBr₄, and (f) (oPDA)₄(PbBr₄)₂Pb₃Br₁₀•4H₃PO₂, respectively. Spectral analysis is indicated by the color dots as indicated in the structures shown in (a). All spectra were acquired at 18.8 T (¹H = 800.1 MHz, ²⁰⁷Pb = 167.4 MHz), with 50 kHz MAS at room temperature.

distortion and bond angle variance for the compounds are listed in Table 2. For 2D structures, the degree of bond angle variance and bond length distortion, in descending order, are 2D (mPDA)PbBr₄ > 2D (pPDA)PbBr₄. Thus, the asymmetric arrangement of NH₃ $^+$ groups (meta) in the aromatic diammonium ions exerts larger octahedra tilting compared to the symmetric cases (para). The bond angle and bond length variances of 1D (oPDA)₄(PbBr₄)₂Pb₃Br₁₀·4H₃PO₂ are smaller than those of 2D compounds.

2.2. Cation–Anion Interactions. Hydrogen bonding plays an important role in stabilizing octahedral tilting and inducing structural distortion. Further insights into hydrogen-bonding interactions have been drawn from the single-crystal structures. For 2D (pPDA)PbBr₄, the short distances of H···Br are \sim 2.59, \sim 2.72, and \sim 2.88 Å, as shown in Figure 4a. Similarly, the distances of H···Br (\sim 2.49 and \sim 2.55 Å) for 2D (mPDA)PbBr₄ are considerably shorter than those of 2D (pPDA)PbBr₄ (Figure 4b). Thus, the stronger hydrogen-bonding interactions in (mPDA)PbBr₄ might induce a larger distortion than that of (pPDA)PbBr₄, which is in line with the analysis of crystal structure discussed above.

Considering the two 1D compounds have a similar structure, we choose 1D (oPDA)₄(PbBr₄)₂Pb₃Br₁₀·4H₃PO₂ for comparison in the following discussion. In 1D (oPDA)₄(PbBr₄)₂Pb₃Br₁₀·4H₃PO₂ structure, the two sides of the ammonium cations can form hydrogen-bonding interactions with the H₃PO₂ molecules as well as bromide anions. Although the two sides of the ammonium cations can form hydrogen-bonding interactions with bromide anions, one H····Br bond is formed with one edge-sharing chain and the other one with two edge-sharing chains. The amino groups in the oPDA cations are tightly bound with these two kinds of chains, not with the same chain (Figure 4c). Thus, the amino groups of oPDA cations are too close to bridge with the same adjacent inorganic sheets simultaneously and unable to stabilize the 2D perovskite structures.

2.3. Short-Range Structures through Solid-State NMR

Analysis. To further understand the organic layer and its impact on the organic-inorganic interfacial structure in these materials, we employed solid-state (ss) Nuclear Magnetic Resonance (NMR) spectroscopy. It has been used to gain insight into cation ordering and their dynamics, interfacial engineering, phase stability, and the degradation of products. 41-45 In this study, we used ¹H and ²⁰⁷Pb magic-angle spinning (MAS) NMR spectroscopy to examine the local packing interactions of the three compounds. Particularly, ¹H and ²⁰⁷Pb NMR chemical shifts are sensitive to intermolecular interactions at the organic-inorganic interface, and apical octahedral tilting. 46,47 For para-, meta-, and ortho-diammonium cations (Figure 5a), the different local chemical environments of the proton sites are expected to lead to different frequencies. Figure 5b compares the 1D ¹H NMR spectra of 2D (pPDA)PbBr4, 2D (mPDA)PbBr4, and 1D (oPDA)₄(PbBr₄)₂Pb₃Br₁₀·4H₃PO₂, where the different displacements of ¹H chemical shifts of the -NH₃⁺ groups indicate different hydrogen-bonding interactions with the PbBr₆ octahedra. For (pPDA)PbBr₄, the partially resolved peaks at 9.2 and 8.1 ppm correspond to the -NH₃⁺ (green dots) and aromatic protons (blue dots), respectively. However, the (mPDA)PbBr₄ phase exhibits peaks at 9.7 ppm (-NH₃⁺ protons, green dots), 7.6 ppm (aromatic protons, blue dots), and a partially resolved peak at 6.8 ppm (purple dot) associated with the proton that is in the meta position with respect to -NH3+ groups. By analyzing and comparing the ²⁰⁷Pb chemical shifts, we obtained insight into the organicinorganic interfaces such as apical octahedral tilting and octahedral penetration. In the ²⁰⁷Pb NMR spectra (Figure 5c), the pPDA and mPDA 2D phases displayed peaks at -50 and 50 ppm with a relative difference in the lead shift, $\Delta \delta = 100$ ppm, corroborating the different local chemical environments of PbBr₆ and octahedral tilting.

For these 2D perovskites, the ¹H chemical shift of $-NH_3^+$ site at 9.7 ppm in the mPDA cation suggests stronger hydrogen-bonding interactions with lead bromide octahedra than the pPDA cations with the ¹H chemical shift of $-NH_3^+$ site at 9.2 ppm, which is in line with the analysis of crystal structure discussed above. In contrast, the 1D (oP-DA)₄(PbBr₄)₂Pb₃Br₁₀·4H₃PO₂ displays a peak at 10 ppm associated with $-NH_3^+$ protons (green dots) that involve in hydrogen-bonding interactions with H_3 PO₂. Further, a broad distribution of peaks in the 5.5–9.0 ppm range is due to aromatic protons (blue dots). As mentioned above, the $-NH_3^+$ groups in the oPDA cations cannot develop hydrogen-bonding interactions with the PbBr₆ octahedra from adjacent layers of lead octahedra owing to steric effects, thus forming a 1D phase.

Next, we applied 2D ¹H-¹H double-quantum singlequantum (DQ-SQ) correlation spectroscopy to probe packing interactions within the organic layer. In such experiments, 2D peaks are detected for through-space inter- and intramolecular dipolar-coupled ¹H-¹H pairs within a distance of 5 Å. These manifest as on-diagonal (chemically equivalent protons) and off-diagonal (chemically inequivalent proton sites) signals. The DQ chemical shift appears at the sum of the SQ chemical shifts, yielding to chemical shift dispersion in the vertical DQ axis twice as large as the horizontal SQ axis. The 2D ¹H-¹H DQ-SQ correlation spectra of the three systems show different DQ peaks, which can be attributed to different packing interactions. For 2D (pPDA)PbBr4 (Figure 5d), the ondiagonal ¹H DQ peak at 16.2 ppm corresponds to the intramolecular dipolar interactions between the aromatic protons as depicted by the two blue dots. The off-diagonal DQ peak at 17.5 ppm corresponds to dipolar interactions between -NH3+ and aromatic protons (green and blue, respectively). The on-diagonal peak at 18.8 ppm corresponds to the intramolecular dipolar interaction within the -NH₃+ groups, as represented by the two green dots. The intermolecular contributions to this peak are negligible because the nearest distance between the intermolecular -NH₃+ groups in pPDA cations is 5 Å. In 2D (pPDA)PbBr₄, the intermolecular aromatic H-H proximities are also > 4 Å. By comparison, the ¹H DQ spectrum of 2D (mPDA)PbBr₄ (Figure 5e) exhibits an off-diagonal DQ peak at 14.4 ppm due to the through-space inter- and intramolecular dipolar interactions between the aromatic protons as depicted in blue and purple dots, and the off-diagonal DQ peak at 17.3 ppm is due to the intramolecular through-space proximity between the -NH₃⁺ (green dots) and aromatic protons (blue dots), respectively. The strong intensity on-diagonal ¹H DQ peak at 19.4 ppm is due to the intramolecular dipolar interactions in -NH₃⁺ groups, and the weak intensity on-diagonal ¹H DQ peak at 15.2 ppm is attributable to both inter- and intramolecular ¹H-¹H proximities between aromatic protons that are in meta position with respect to each other (blue dots) for which the interatomic distance is \sim 4 Å.

For the 1D $(oPDA)_4(PbBr_4)_2Pb_3Br_{10}\cdot 4H_3PO_2$ system (Figure 5f), we observed a broad distribution of the DQ peak at ~15 ppm, corresponding to intra- and intermolecular interactions between the aromatic protons depicted by the two blue dots. The broad signals are due to the substantial self-assembly by oPDA cations, which lead to one-to-one as well as slip-stacked dimers, resulting in different $\pi-\pi$ stacking and $C-H-\pi$ interactions. For example, the hydrogen atoms depicted in the blue and red dots exhibit different aromatic ring current effects, leading to a broad distribution of peaks in the 6–9 ppm

range. A weak off-diagonal DQ peak further corroborates this at 17.6 ppm that originates from intermolecular dipolar interactions between the aromatic (blue dots) and $-\mathrm{NH_3}^+$ protons (green dots) for which the intermolecular $^1\mathrm{H}-^1\mathrm{H}$ distance is ~ 3.1 Å. In addition, the distinct on-diagonal DQ peaks at 20.2 ppm are ascribed to the intramolecular dipolar interactions between the adjacent $-\mathrm{NH_3}^+$ protons depicted by the two green dots. These structural differences contribute to different optical and electronic properties, as discussed below.

2.4. Optical Properties, White-Light Emission, and Work Functions. The optical absorption spectra of the three compounds are shown in Figure 6a. 2D (pPDA)PbBr₄ and

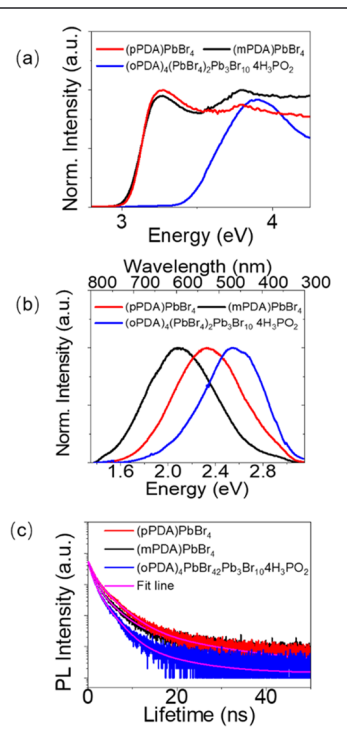


Figure 6. (a) Optical absorption spectra, (b) steady-state PL spectra, and (c) time-resolved PL spectra for 2D (pPDA)PbBr₄, 2D (mPDA)PbBr₄, and 1D (oPDA)₄(PbBr₄)₂Pb₃Br₁₀·4 H₃PO₂, respectively.

(mPDA)PbBr₄ show sharp absorption edges and well-defined excitonic peaks, respectively. Strong quantum and dielectric confinement effects owing to the organic spacers in 2D perovskites give rise to tightly bound excitons with large binding energies. Because of the excitonic peaks, it was difficult to determine the correct band gaps for the compounds. The energies of the absorption edges are listed in Table 2. The absorption edge of 3.44 eV for 1D (oPDA)₄(PbBr₄)₂Pb₃Br₁₀· 4H₃PO₂ is significantly larger than that of 2D perovskite compounds. This is consistent with the fact that the metal octahedra share edges in the 1D structure compared to the corner-sharing motif in perovskite structures.

Although the optical spectra show sharp absorption edges, the photoluminescence (PL) spectra of all of the compounds exhibit broadband emission features, as shown in Figure 6b. For 2D (mPDA)PbBr₄, the maximum of PL peak is centered at 2.08 eV and the PL emission exhibits the broadest peak from 2.47 eV (502 nm) to 1.74 eV (713 nm) (full width at half-maximum (FWHM):0.73 eV (211 nm)) due to the largest octahedra distortion. For 2D (pPDA)PbBr₄, the maximum of

PL peak is centered at 2.35 eV and the PL peak exhibits the second broader peak with an FWHM of 0.69 eV (158 nm) (from 2.70 eV (459 nm) to 2.01 eV (617 nm)). It has been argued that the broad photoluminescence (PL) emission is associated with a high level of bond length distortion of the structure. ^{16,50} It is noteworthy to draw comparison to the published structure of the lead iodide analogues. The 2D (pPDA)PbI₄ cannot be stabilized with pPDA cation, but the synthesis and photophysical characterization of 2D (mPDA)PbI₄ were previously reported in our group. ⁵¹ Although the average Pb—I—Pb angle for 2D (mPDA)PbI₄ is 143.8°, similar to that in (mPDA)PbBr₄ (Table 2), the bond length distortion of the octahedron in 2D (mPDA)PbI₄ is smaller than in (mPDA)PbBr₄. This could be linked to the narrower PL emission of 2D (mPDA)PbI₄ than that of (mPDA)PbBr₄.

The 1D (oPDA)₄(PbBr₄)₂Pb₃Br₁₀·4H₃PO₂ compound exhibits a narrow PL peak at 2.58 eV with an FWHM of 0.62 eV. The optical properties of the 1D (oPDA)₂Pb₃Br₁₀ structures are shown in Figures S2 and S3. The broad PL emission for 1D (oPDA)₂Pb₃Br₁₀ might be attributed to the relatively larger bond length distortion than 1D (oPDA)₄(PbBr₄)₂Pb₃Br₁₀·4H₃PO₂. From time-resolved PL experiments (Figure 6c), we observe that the average lifetimes for 2D (pPDA)PbBr₄, 2D (mPDA)PbBr₄, and 1D (oPDA)₄(PbBr₄)₂Pb₃Br₁₀·4H₃PO₂ are 3.05, 3.17, and 1.72 ns, respectively (Table 3), which is an

Table 3. Summary of PL Average Lifetimes for 2D (pPDA)PbBr₄, 2D (mPDA)PbBr₄, and 1D (oPDA)₄(PbBr₄)₂Pb₃Br₁₀·4H₃PO₂ with Estimated Standard Deviations in Parentheses

	$ au_1$	$ au_2$	$ au_3$	$ au_{ ext{average}}$ (ns)
(pPDA)PbBr ₄	0.98	3.07	12.87	3.17
(mPDA)PbBr ₄	0.99	3.08	15.89	3.05
$(oPDA)_4(PbBr_4)_2Pb_3Br_{10}4H_3PO_2$	0.78	2.27	8.99	1.72
(pPDA)PbBr ₄ film	0.67	3.01	19.57	3.16
(mPDA)PbBr ₄ film	0.81	2.75	15.82	1.93
$ \begin{array}{c} (\text{oPDA})_4 (\text{PbBr}_4)_2 \text{Pb}_3 \text{Br}_{10} \text{4H}_3 \text{PO}_2 \\ \text{film} \end{array} $	0.73	2.64	20.23	1.88

indication of slower carrier recombination and improved carrier transport for 2D compounds compared to the 1D system.⁵² The measured average lifetime of each sample was fitted using a three-exponent function (details are provided in the Experimental Section).

These low-dimensional perovskites with short rigid conjugated spacer dications can achieve large-scale tunability in the chromaticity of emission. The chromaticity diagram (CIE) and correlated color temperature (CCT) are obtained using the color calculator software (OSRAM Sylvania, Inc.), as shown in Figure 7. Their coordinates deviate from the white point (0.33, 0.33), as shown in Table 2.53 The photos of light emissive samples are captured under UV illumination (TOC). The CCT below 4500 K can produce neutral warm-white light. The (mPDA)PbBr₄ has a CIE coordinate of (0.44, 0.46), which has a reddish-white emission compared to the white point at (0.33, 0.33). The CIE of (pPDA)PbBr₄ and 1D $(oPDA)_4(PbBr_4)_2Pb_3Br_{10}\cdot 4H_3PO_2$ are (0.34, 0.44) and (0.21, 0.29), respectively, and they give CCT of 5450 and >10,000 K, respectively. Thus, they emit cold-white light. To further explore the mechanism of the broadband emission, we performed variable-temperature PL from 80 to 290 K for 2D (mPDA)PbBr₄ and (pPDA)PbBr₄ compounds (Figure S4).

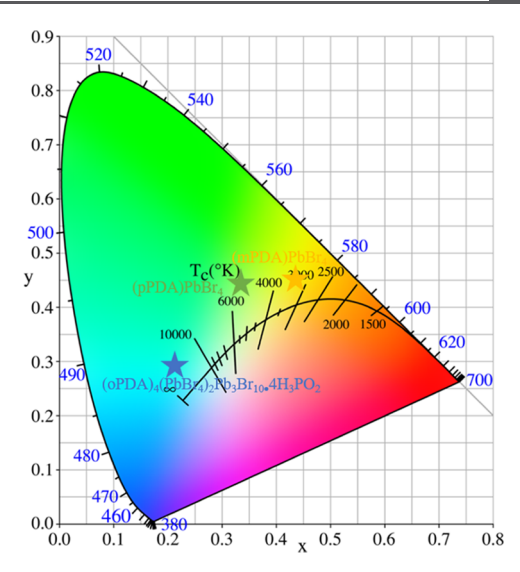


Figure 7. CIE color coordinates of (pPDA)PbBr₄, (mPDA)PbBr₄, and (oPDA)₄(PbBr₄)₂Pb₃Br₁₀·4H₃PO₂ in 1931 color space chromaticity diagram. The chromaticity coordinates (x, y), CCT, and CRI are calculated using the Color Calculator software (OSRAM Sylvania, Inc.).

Both the PL spectra present a significant red shift, decreased PL intensity, and broadening of the PL peak with increasing temperature. Thus, trap-mediated excitonic recombination or self-trapped excitons (STEs) might also contribute to the broadband emission.^{54,55}

Considering these newly synthesized perovskite compounds could be used in future devices, it is important to know the energy positions of their valence and conduction bands in terms of the correct interface and device assembly. The valence band maximum (VBM) of the different compounds was measured by photoemission yield spectroscopy in air (PYS) (Figure 8a-d). Here we should mention that the conduction band minimum (CBM) is calculated from the difference between the VBM and the band gap. There might be an underestimation on the order of a few hundred meV due to the existence of exciton binding energy in the 2D perovskite material.⁵⁶ We also compare the VBM and CBM of the three compounds with those of PbBr₂ and 3D MAPbBr₃ perovskite. 19 The three compounds have a strong energy variation in the CBM (2.57 eV for (mPDA)PbBr4, 2.51 eV for (pPDA)-PbBr₄, and 2.04 eV for 1D (oPDA)₄(PbBr₄)₂Pb₃Br₁₀·4H₃PO₂), whereas the VBMs (5.49 eV for (mPDA)PbBr₄, 5.54 eV for (pPDA)PbBr₄, and 5.52 eV for 1D (oPDA)₄(PbBr₄)₂Pb₃Br₁₀· 4H₃PO₂) remain almost constant. Compared with those of PbBr₂ and 3D MAPbBr₃, the VBM for the three compounds is similar to that of 3D MAPbBr₃, while the VBM for the three compounds is between those of PbBr₂ and 3D MAPbBr₃. Thus, the different cations significantly influence the VBM and CBM, which is an important factor for the correct interface assembly.

2.5. Electronic Band Structure Calculations. The electronic band structures of (pPDA)PbBr₄ and (mPDA)-PbBr₄ are shown in Figure 9a,b. Both 2D materials are direct-band-gap semiconductors at the Γ point of the Brillouin zone. Employing the hybrid functional PBE0, which is known to correct the DFT underestimated band-gap values, ^{57,58} we calculated the electronic band gaps of 3.40 eV for (pPDA)-PbBr₄ and (mPDA)PbBr₄, slightly larger than the 3.11 eV electronic band gap of the prototypical Ruddlesden—Popper

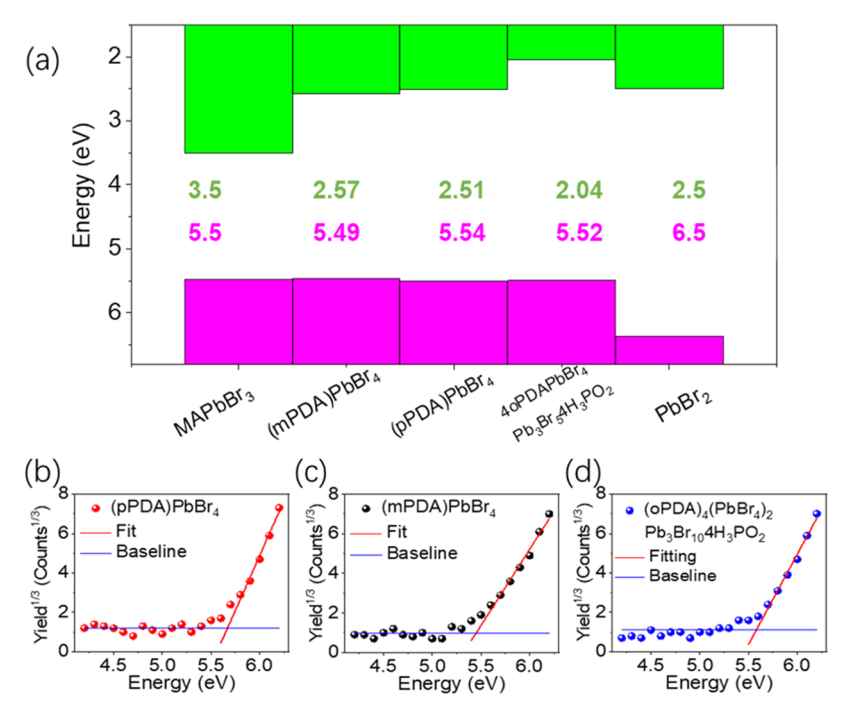


Figure 8. (a) Experimental energy band alignment (VBM and CBM) of lead bromide compounds of (pPDA)PbBr₄, (mPDA)PbBr₄, and (oPDA)₄(PbBr₄)₂Pb₃Br₁₀·4H₃PO₂ compared with that of the 3D MAPbBr₃ and PbBr₂. Work function measurement for (b) 2D (pPDA)PbBr₄, (c) 2D (mPDA)PbBr₄, and (d) 1D (oPDA)₄(PbBr₄)₂Pb₃Br₁₀·4H₃PO₂, respectively.

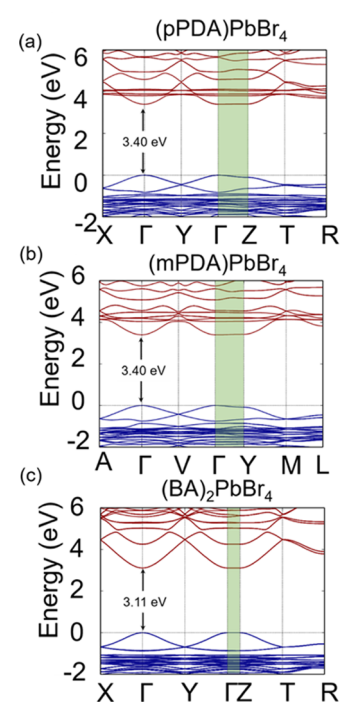


Figure 9. Electronic structure for the 2D compounds: (a) (pPDA)PbBr₄, (b) (mPDA)PbBr₄, and prototypical layered perovskite (c) (BA)₂PbBr₄. The band gap is calculated employing the hybrid exchange-correlation functional PBE0. The direction that corresponds to the layer stacking is highlighted in green.

layered perovskite $(BA)_2PbBr_4$. For 1D (oP-DA)₄(PbBr₄)₂Pb₃Br₁₀·4H₃PO₂, the band gap is indirect (Figure S5), and larger (4.11 eV within PBE0) than the 2D materials, in agreement with the experiments. The difference between the calculated band gaps matches the trend observed

in the optical absorption spectra (vide infra). As expected, the Pb s-orbitals and Br p-orbitals contribute to the VBM, while the conduction band minimum (CBM) is composed of mainly Pb p-orbitals (Figure S6). The organic spacer layers, whose states are shown by flat nondispersive bands, do not contribute to the band edges; However, for the 2D compounds, a few organic electronic states are found above the CBM, in contrast to the reference 2D compound (BA)₂PbBr₄.³⁵

The out-of-plane interactions between halogens of adjacent inorganic slabs of 2D perovskite materials are known to play a crucial role in the electronic band structure, especially in iodides. 59,60 To quantify this effect, we calculated the VBM and CBM band dispersion along the stacking direction for the 2D materials, as shown in green in Figure 9a-c. For the VBM of (pPDA)PbBr₄ and (mPDA)PbBr₄, we found small dispersions of 110 and 83 meV, respectively, while for the CBM 18 and 21 meV, within the DFT-PBE0. This is not the case for (BA)₂PbBr₄, for which the dispersion is 0 because the apical interlayer bromines are too far away to interact. Finally, to explore the intralayer charge carrier transport of the 2D materials, we calculated their in-plane effective masses for holes and electrons and compared them to those of (BA)₂PbBr₄. The effective masses of (pPDA)PbBr₄ and (mPDA)PbBr₄ are found slightly larger, $m_e = 0.36$ and 0.34 and $m_h = 0.53$ and 0.50 $m_{\rm e}$, than those for $({\rm BA})_2{\rm PbBr_4}$, $m_{\rm e} = 0.19$ and $m_{\rm h} = 0.33$ m_e. This observation is consistent with the larger in-plane distortions of the Pb-Br octahedra.

Our results show that the observed distortions of layered halide perovskites tend to increase the band gap and the inplane hole and electron effective masses. White-light emission and its observed correlation with structural distortions cannot be explained by the electronic structures of the ideal (pPDA)PbBr₄ and (mPDA)PbBr₄. Other physical mechanisms underly the observed emission, such as exciton trapping facilitated by distortions in the inorganic parts of the

structures, are implied by the results of the temperature-dependent PL spectra of (pPDA)PbBr₄ and (mPDA)PbBr₄ (Figure S4).

2.6. Film Properties and Stability. Most perovskite films reported previously were made from mixtures of the precursor components. Herein, we dissolve the single crystals directly in the solvent, and the memory seeds could enable high structural phase purity in the 2D perovskite film. Notably, the (pPDA)PbBr₄ compounds form a clear N_iN_i -DMF solution, but a dark blue solution forms in dimethyl sulfoxide (DMSO). The 2D (pPDA)PbBr₄ cannot dissolve in acetonitrile (ACN) and γ -butyrolactone (GBL) (Figure S7). Thus, all three crystals are dissolved in anhydrous DMF. The details of the film assembly are described in the Experimental Section.

The XRD patterns of the films (Figure 10a) exhibit lowangle basal Bragg peaks below $2\theta = 10^{\circ}$, similar to the powder

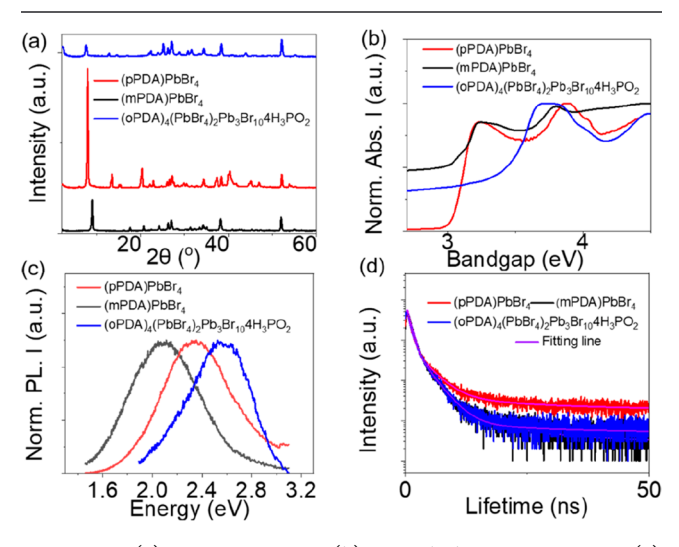


Figure 10. (a) PXRD patterns, (b) optical absorption spectra, (c) steady-state PL spectra, and (d) time-resolved PL spectra for 2D (pPDA)PbBr₄, 2D (mPDA)PbBr₄, and 1D (oPDA)₄(PbBr₄)₂Pb₃Br₁₀· 4 H₃PO₂ films, respectively.

XRD pattern of single-crystal materials. The optical absorption spectra (Figure 10b) confirm the formation of 2D perovskite pure phases for (pPDA)PbBr₄ and (mPDA)PbBr₄ films. For 1D (oPDA)₄PbBr₄Pb₃Br₅·4H₃PO₂, the absorption edge is 3.45 eV, which is also similar to the material itself. The PL from the 2D (pPDA)PbBr₄ and (mPDA)PbBr₄ films still show broad emission (Figure 10c). In addition, all of the average lifetimes are comparable to the bulk materials at 1.93, 3.17, and 1.88 ns for 2D (pPDA)PbBr₄, 2D (mPDA)PbBr₄, and 1D (oPDA)₄(PbBr₄)₂Pb₃Br₁₀·4H₃PO₂ films, respectively (Figure 10d and Table 3).

We also investigated the stability of the three-hybrid lead bromide perovskite films to assess their potential in devices (Figure S8). We used a continuous UV irradiation illumination test in the air (temperature, 22 °C; humidity, 35%). All of the color and XRD results for the three films remain constant for more than 24 h. The long-term thermal stability test was conducted on a hot plate at 80 °C in the air (temperature 22 °C, humidity 35%). According to the XRD results, only the (mPDA)PbBr4 films remain stable during continuous heating in air for more than 24 h. We find splitting in the low-angle (2θ < 10°) Bragg peaks for the other two cases, suggesting the

structural decomposition. The color for the (pPDA)PbBr₄ films changes from white to dark gray, and light pink for the 1D (oPDA)₄(PbBr₄)₂Pb₃Br₁₀·4H₃PO₂ films, after 24 h heating in air. Thus, the (mPDA)PbBr₄ films exhibit the best thermal stability due to the stronger hydrogen-bonding interactions in its structure.

3. CONCLUSIONS

The influence of ammonium group positions in the short rigid aromatic moiety of phenylene diammonium family on the crystal structures of low-dimensional lead bromides is strong and leads to 2D perovskite and 1D nonperovskite motifs all with broad white-light emission. When the amino groups are in the meta and para positions, the aromatic diammonium cations allow the formation of 2D network perovskite structures (n =1). When in the ortho positions, the cations stabilize only 1D structures. New insights into the local packing arrangements of organic spacers and organic-inorganic interfaces are obtained using high-field ¹H and ²⁰⁷Pb solid-state 2D-NMR spectroscopy. The (pPDA)PbBr₄ and (mPDA)PbBr₄ perovskite exhibit different ammonium group penetrations and hydrogenbonding interactions, which modulate the Br-Pb-Br bond angles and the tilting of the corner-sharing PbBr₆ octahedra. The NMR shows a large difference in the ^{207}Pb ($\Delta\delta \sim 100$ ppm) and ¹H chemical shifts of the $-NH_3^+$ groups ($\Delta\delta \sim 0.5$ ppm), among the compounds reflecting the local PbBr₆ distortions. We also find structure-PL correlations, which link the level of the bond length distortions in the inorganic [PbBr₄]²⁻ layer to the broad bandwidth of the PL emission. The bond length distortions for the three compounds in descending order are 2D (mPDA)PbBr₄ > 2D (pPDA)PbBr₄ >1D (oPDA)₄PbBr₄Pb₃Br₅·4H₃PO₂. Consequently, 2D (mPDA)PbBr₄ compounds exhibit the broadest white-light emission, while the narrowest white emission is observed for 1D (oPDA)₄PbBr₄Pb₃Br₅·4H₃PO₂. Density functional theory calculations for 2D (mPDA)PbBr₄ and 2D (pPDA)PbBr₄ suggests direct band gaps with relatively broad valence and conduction bands along the in-plane directions, but a slightly indirect band gap for the 1D (oPDA)₄PbBr₄Pb₃Br₅·4H₃PO₂. The (mPDA)PbBr₄ film exhibits better thermal stability in ambient air than the other two films, presumably because of the stronger hydrogen-bonding interactions in the material. Therefore, our findings support the general belief that tuning the structural distortion in low-dimensional perovskites based on the shape and size of the spacer cation is an effective handle for designing single-source white-light emitters.

4. EXPERIMENTAL SECTION

4.1. Synthesis of 2D (pPDA)PbBr₄, 2D (mPDA)PbBr₄, 1D (oPDA)₄(PbBr₄)₂Pb₃Br₁₀·4 H_3 PO₂, and 1D (oPDA)₂Pb₃Br₁₀. 4.1.1. For (pPDA)PbBr₄. PbO powder (n=446.4 mg, 2 mmol) was dissolved in 5 mL of hydrobromic acid and 1 mL of H_3 PO₂ solution (or without 1 mL of H_3 PO₂) by heating, with constant stirring for 5–10 min at ~200 °C until the solution became clear. Then, 64.9 mg (0.6 mmol) of pPDA was added directly to the above solution under the same conditions until complete dissolution. Finally, the solution was cooled to 120 °C and eventually to room temperature to obtain white platelike crystals of pPDAPbBr₄. The product was isolated by suction filtration followed by drying in a filtration funnel for 30 min. The yield obtained was 750 mg (58.9% of total Pb content).

4.1.2. For (mPDA)PbBr₄. PbO powder (n = 446.4 mg, 2 mmol) was dissolved in 3 mL of hydrobromic acid and 1 mL of H₃PO₂ solution (or without 1 mL of H₃PO₂) by heating with constant stirring for 5–10 min at ~200 °C until the solution became clear. Then, 64.9 mg

(0.6 mmol) of mPDA was added directly to the above solution under the same conditions until complete dissolution. Finally, the solution was cooled to 120 $^{\circ}$ C and eventually to room temperature to obtain white platelike crystals of mPDAPbBr₄. The product was isolated by suction filtration followed by drying in a filtration funnel for 30 min. The yield obtained was 366 mg (28.7% of the total Pb content).

4.1.3. For $(oPDA)_4(PbBr_4)_2Pb_3Br_{10}\cdot 4H_3PO_2$. PbO powder (446.4 mg, 2 mmol) was dissolved in 3 mL of hydrobromic acid and 1 mL of H_3PO_2 solution by heating with constant stirring for 5–10 min at ~200 °C until the solution became clear. The only difference for 1D $(oPDA)_4Pb_3Br_{10}$ was the absence of 1 mL of H_3PO_2 . Next, 64.9 mg (0.6 mmol) of oPDA was added directly to the above solution with the same conditions until complete dissolution. Finally, the solution was cooled to 120 °C and crystals were obtained at room temperature. The product was isolated by suction filtration followed by drying in a filtration funnel for 30 min. The yield obtained was 186 mg (14.6% of total Pb content).

4.2. Film Fabrication. FTO glass substrates were first cleaned by sequential sonication in acetone and isopropanol for 15 min each. Subsequently, the FTO substrates were dried with nitrogen and treated for 30 min using ultraviolet ozone (UVO). Solutions of the studied materials were prepared by dissolving 100 mg of dried crystals in 200 μ L of anhydrous DMF solvent. The substrates were heated at 110 °C on a hot plate for 10 min under N₂ atmosphere. Then, the precursor solution was spin-coated at 5000 rpm for 30 s in a glovebox under a N₂ atmosphere.

4.2.1. Single-Crystal X-ray Crystallography. Single-crystal XRD experiments were performed using a STOE IPDS II or IPDS 2T diffractometer with Mo K α radiation (λ = 0.71073 Å) operating at 50 kV and 40 mA. Integration and numerical absorption corrections were performed using X-AREA, X-RED, and XSHAPE programs. The structures were solved by charge flipping and refined using the full-matrix least squares in Olex2. The PLATON software was used to identify the twinning domains and validate the space groups of the compounds.

4.2.2. Solid-State NMR Spectroscopy. All solid-state magic-angle spinning (MAS) NMR experiments were carried out using an 18.8 T (1H, 800.1 MHz) Bruker Avance Neo NMR spectrometer equipped with a 1.3 mm H-X probe head. Single-crystal samples of the 1D and 2D perovskites and precursor salts were separately packed into 1.3 mm zirconia rotors (outer diameter) fitted with VESPEL caps. Unless otherwise specified, all of the samples were spun at a MAS frequency of 50 kHz. ¹H relaxation delays were determined from the saturation recovery measurements and analyses. Single-pulse ¹H MAS NMR spectra were acquired by co-addition of 32 transients. The 1D ²⁰⁷Pb MAS experiments were carried out using a spin-echo pulse sequence. Each spectrum was acquired with 4096 co-added transients using a relaxation delay of 800 ms. For all compounds, 2D ¹H-¹H doublequantum (DQ)-single-quantum (SQ) NMR spectra were acquired using a back-to-back sequence under fast MAS.⁶³ A rotorsynchronized t_1 increment of 20 μ s was applied with a DQ excitation time of 40 μ s corresponding to two rotor periods ($2\tau_r$). The ¹H DQ dimensions were acquired using 128 t_1 FIDs, each with 16 co-added transients. The ¹H experimental spectra were calibrated with respect to that of neat TMS using adamantane as an external reference (1H resonance, 1.82 ppm). 207Pb experimental shift was calibrated with respect to neat liquid Pb(NO₃)₂ based on IUPAC recommendation.

ASSOCIATED CONTENT

Supporting Information

The Supporting Information is available free of charge at https://pubs.acs.org/doi/10.1021/acs.chemmater.2c02471.

Additional experimental details, materials, and methods; calculated/experimental XRD patterns, optical absorption spectra, steady-state PL spectra, and projected density of states (PDOS) and detailed single-crystal information for all compounds; electronic structure for the 1D compounds; temperature-dependent photo-

luminescence spectra for 2D compounds; and film stability of all compounds, including photographs of different solutions (PDF)

Accession Codes

CCDC 2182661-2182664 contain the supporting crystallographic data for this paper.

AUTHOR INFORMATION

Corresponding Author

Mercouri G. Kanatzidis — Department of Chemistry, Northwestern University, Evanston, Illinois 60208, United States; orcid.org/0000-0003-2037-4168; Email: mkanatzidis@northwestern.edu

Authors

Ping Fu — State Key Laboratory of Catalysis, Dalian Institute of Chemical Physics, Chinese Academy of Sciences, Dalian National Laboratory for Clean Energy, Dalian 116023, China; Department of Chemistry, Northwestern University, Evanston, Illinois 60208, United States; orcid.org/0000-0002-7454-5754

Michael A. Quintero — Department of Chemistry, Northwestern University, Evanston, Illinois 60208, United States: Oorcid.org/0000-0002-0709-1676

Claire Welton – University of Lille, CNRS, Centrale Lille Institute, Univ. Artois, UMR 8181–UCCS – Unité de Catalyse et Chimie du Solide, F-59000 Lille, France

Xiaotong Li − Department of Chemistry, Northwestern University, Evanston, Illinois 60208, United States; orcid.org/0000-0001-7107-7273

Bruno Cucco – Univ Rennes, ENSCR, INSA Rennes, CNRS, ISCR (Institute des Sciences Chimiques de Rennes), UMR 6226, F-35000 Rennes, France

Michael C. De Siena – Department of Chemistry, Northwestern University, Evanston, Illinois 60208, United States; © orcid.org/0000-0003-0379-5577

Jacky Even – Univ Rennes, INSA Rennes, CNRS, Institute FOTON - UMR 6082, F-35000 Rennes, France;
orcid.org/0000-0002-4607-3390

George Volonakis — Univ Rennes, ENSCR, INSA Rennes, CNRS, ISCR (Institute des Sciences Chimiques de Rennes), UMR 6226, F-35000 Rennes, France; orcid.org/0000-0003-3047-2298

Mikaël Kepenekian — Univ Rennes, ENSCR, INSA Rennes, CNRS, ISCR (Institute des Sciences Chimiques de Rennes), UMR 6226, F-35000 Rennes, France; ○ orcid.org/0000-0001-5192-5896

Runze Liu — State Key Laboratory of Molecular Reaction Dynamics and Dynamics Research Center for Energy and Environmental Materials, Dalian Institute of Chemical Physics, Chinese Academy of Sciences, Dalian 116023, China

Craig C. Laing – Department of Chemistry, Northwestern University, Evanston, Illinois 60208, United States;
ocid.org/0000-0002-0654-4741

Vladislav Klepov – Department of Chemistry, Northwestern University, Evanston, Illinois 60208, United States

Yukun Liu – Department of Materials Science and Engineering, Northwestern University, Evanston, Illinois 60208, United States

Vinayak P. Dravid — Department of Materials Science and Engineering, Northwestern University, Evanston, Illinois 60208, United States; orcid.org/0000-0002-6007-3063

- G. N. Manjunatha Reddy Department of Chemistry, Northwestern University, Evanston, Illinois 60208, United States; University of Lille, CNRS, Centrale Lille Institute, Univ. Artois, UMR 8181—UCCS — Unité de Catalyse et Chimie du Solide, F-59000 Lille, France; orcid.org/0000-0002-8283-2462
- Can Li State Key Laboratory of Catalysis, Dalian Institute of Chemical Physics, Chinese Academy of Sciences, Dalian National Laboratory for Clean Energy, Dalian 116023, China; orcid.org/0000-0002-9301-7850

Complete contact information is available at: https://pubs.acs.org/10.1021/acs.chemmater.2c02471

Author Contributions

P.F. and M.A.Q. contributed equally to this work. P.F. performed sample synthesis, structural characterization, and optical measurements, and wrote the paper. M.Q. and V.K. helped refine the single-crystal structure. C.W. and G.N.M. Reddy carried out the solid-state NMR measurements and analyses. B.C., G.V., J.E., M.K., and R.L. performed density functional theory calculations. M.D.S. trained the PL instrument, and Y.L. and V.D. performed the SEM analyses. C.L. performed the work function test. X.L. discussed the synthesis and revised the manuscript accordingly. C.L. revised the manuscript. M.G.K. supervised the study and revised the manuscript. The manuscript reflects the contributions of all of the authors.

Notes

The authors declare no competing financial interest.

ACKNOWLEDGMENTS

This work was supported by the National Science Foundation under Grant No. DMR-2019444 (IMOD an NSF-STC). This work used the NUFAB facility of Northwestern University's NUANCE Center, which has received support from the SHyNE Resource (NSF ECCS-2025633), the IIN, the Northwestern MRSEC program (NSF DMR-1720139), the MRSEC program (NSF DMR-1720139) at the Materials Research Center, the International Institute for Nanotechnology (IIN), the Keck Foundation, and the State of Illinois through IIN. G.N.M.R. gratefully acknowledges financial support from ISITE international mobility grant, IR INFRANALYTICS FR2054, and EU H2020 (Grant 795091) for conducting the ssNMR experiments. P.F. acknowledges the financial support from the Chinese Academy of Science as a visiting scholar at Northwestern University, USA, 2020RQ036, and fruitful discussion with Chenjian Lin, Yanfeng Yin, and Paige Brown.

REFERENCES

- (1) Fu, P.; Qin, W.; Bai, S. Q.; Yang, D.; Chen, L. D.; Guo, X.; Li, C. Integrating large-area perovskite solar module with thermoelectric generator for enhanced and stable power output. *Nano Energy* **2019**, 65, No. 104009.
- (2) Yang, W. S.; Park, B. W.; Jung, E. H.; Jeon, N. J.; Kim, Y. C.; Lee, D. U.; Shin, S. S.; Seo, J.; Kim, E. K.; Noh, J. H.; Seok, S. I. Iodide management in formamidinium-lead-halide-based perovskite layers for efficient solar cells. *Science* **2017**, *356*, 1376–1381.
- (3) Correa-Baena, J. P.; Saliba, M.; Buonassisi, T.; Gratzel, M.; Abate, A.; Tress, W.; Hagfeldt, A. Promises and challenges of perovskite solar cells. *Science* **2017**, *358*, 739–744.

- (4) Kojima, A.; Teshima, K.; Shirai, Y.; Miyasaka, T. Organometal Halide Perovskites as Visible-Light Sensitizers for Photovoltaic Cells. *J. Am. Chem. Soc.* **2009**, *131*, 6050–6055.
- (5) Stranks, S. D.; Snaith, H. J. Metal-halide perovskites for photovoltaic and light-emitting devices. *Nat. Nanotechnol.* **2015**, *10*, 391–402.
- (6) Yuan, M. J.; Quan, L. N.; Comin, R.; Walters, G.; Sabatini, R.; Voznyy, O.; Hoogland, S.; Zhao, Y. B.; Beauregard, E. M.; Kanjanaboos, P.; Lu, Z. H.; Kim, D. H.; Sargent, E. H. Perovskite energy funnels for efficient light-emitting diodes. *Nat. Nanotechnol.* **2016**, *11*, 872–876.
- (7) Stoumpos, C. C.; Malliakas, C. D.; Kanatzidis, M. G. Semiconducting Tin and Lead Iodide Perovskites with Organic Cations: Phase Transitions, High Mobilities, and Near-Infrared Photoluminescent Properties. *Inorg. Chem.* **2013**, *52*, 9019–9038.
- (8) Ahmad, S.; Fu, P.; Yu, S. W.; Yang, Q.; Liu, X.; Wang, X. C.; Wang, X. L.; Guo, X.; Li, C. Dion-Jacobson Phase 2D Layered Perovskites for Solar Cells with Ultrahigh Stability (vol 3, pg 794, 2019). *Joule* **2019**, *3*, 889–890.
- (9) Tsai, H. H.; Nie, W. Y.; Blancon, J. C.; Toumpos, C. C. S.; Asadpour, R.; Harutyunyan, B.; Neukirch, A. J.; Verduzco, R.; Crochet, J. J.; Tretiak, S.; Pedesseau, L.; Even, J.; Alam, M. A.; Gupta, G.; Lou, J.; Ajayan, P. M.; Bedzyk, M. J.; Kanatzidis, M. G.; Mohite, A. D. High-efficiency two-dimensional Ruddlesden-Popper perovskite solar cells. *Nature* **2016**, *536*, 312–318.
- (10) Li, X. T.; Hoffman, J. M.; Kanatzidis, M. G. The 2D Halide Perovskite Rulebook: How the Spacer Influences Everything from the Structure to Optoelectronic Device Efficiency. *Chem. Rev.* **2021**, *121*, 2230–2291.
- (11) Mao, L. L.; Ke, W. J.; Pedesseau, L.; Wu, Y. L.; Katan, C.; Even, J.; Wasielewski, M. R.; Stoumpos, C. C.; Kanatzidis, M. G. Hybrid Dion-Jacobson 2D Lead Iodide Perovskites. *J. Am. Chem. Soc.* **2018**, 140, 3775–3783.
- (12) Ke, W. J.; Mao, L. L.; Stoumpos, C. C.; Hoffman, J.; Spanopoulos, I.; Mohite, A. D.; Kanatzidis, M. C. Compositional and Solvent Engineering in Dion-Jacobson 2D Perovskites Boosts Solar Cell Efficiency and Stability. *Adv. Energy Mater.* **2019**, *9*, No. 1803384.
- (13) Li, W. B.; Sidhik, S.; Traore, B.; Asadpour, R.; Hou, J.; Zhang, H.; Fehr, A.; Essman, J.; Wang, Y. F.; Hoffman, J. M.; Spanopoulos, I.; Crochet, J. J.; Tsai, E.; Strzalka, J.; Katan, C.; Alam, M. A.; Kanatzidis, M. G.; Even, J.; Blancon, J. C.; Mohite, A. D. Light-activated interlayer contraction in two-dimensional perovskites for highefficiency solar cells. *Nat. Nanotechnol.* **2022**, *17*, 45–50.
- (14) Qian, J. Y.; Guo, Q.; Liu, L. J.; Xu, B.; Tian, W. J. A theoretical study of hybrid lead iodide perovskite homologous semiconductors with 0D, 1D, 2D and 3D structures. *J. Mater. Chem. A* **2017**, *5*, 16786–16795.
- (15) Dohner, E. R.; Hoke, E. T.; Karunadasa, H. I. Self-Assembly of Broadband White-Light Emitters. J. Am. Chem. Soc. 2014, 136, 1718—1721.
- (16) Mao, L. L.; Wu, Y. L.; Stoumpos, C. C.; Wasielewski, M. R.; Kanatzidis, M. G. White-Light Emission and Structural Distortion in New Corrugated Two-Dimensional Lead Bromide Perovskites. *J. Am. Chem. Soc.* **2017**, *139*, 5210–5215.
- (17) Thirumal, K.; Chong, W. K.; Xie, W.; Ganguly, R.; Muduli, S. K.; Sherburne, M.; Asta, M.; Mhaisalkar, S.; Sum, T. C.; Soo, H. S.; Mathews, N. Morphology-Independent Stable White-Light Emission from Self-Assembled Two-Dimensional Perovskites Driven by Strong Exciton-Phonon Coupling to the Organic Framework. *Chem. Mater.* 2017, 29, 3947—3953.
- (18) Guo, Y. Y.; Yang, L. J.; Biberger, S.; McNulty, J. A.; Li, T.; Schotz, K.; Panzer, F.; Lightfoot, P. Structural Diversity in Layered Hybrid Perovskites, A(2)PbBr(4) or AA'PbBr4, Templated by Small Disc-Shaped Amines. *Inorg. Chem.* **2020**, *59*, 12858–12866.
- (19) Mao, L. L.; Guo, P. J.; Kepenekian, M.; Hadar, I.; Katan, C.; Even, J.; Schaller, R. D.; Stoumpos, C. C.; Kanatzidis, M. G. Structural Diversity in White-Light-Emitting Hybrid Lead Bromide Perovskites. *J. Am. Chem. Soc.* **2018**, *140*, 13078–13088.

- (20) Yuan, Z.; Zhou, C. K.; Tian, Y.; Shu, Y.; Messier, J.; Wang, J. C.; van de Burgt, L. J.; Kountouriotis, K.; Xin, Y.; Holt, E.; Schanze, K.; Clark, R.; Siegrist, T.; Ma, B. W. One-dimensional organic lead halide perovskites with efficient bluish white-light emission. *Nat. Commun.* **2017**, *8*, No. 14051.
- (21) Lin, H. R.; Zhou, C. K.; Tian, Y.; Siegrist, T.; Ma, B. W. Low-Dimensional Organometal Halide Perovskites. *ACS Energy Lett* **2018**, 3, 54–62.
- (22) Zhao, S. Y.; Jiang, S. Q.; Cai, W. S.; Li, R.; Mo, Q. H.; Wang, B. Q.; Zang, Z. G. Intrinsic white-light emission from low-dimensional perovskites for white-light-emitting diodes with high-color-rendering index. *Cell Rep. Phys. Sci.* **2021**, *2*, No. 100585.
- (23) Sun, S. Q.; Lu, M.; Gao, X. P.; Shi, Z. F.; Bai, X.; Yu, W. W.; Zhang, Y. 0D Perovskites: Unique Properties, Synthesis, and Their Applications. *Adv. Sci.* **2021**, *8*, No. 2102689.
- (24) Yantara, N.; Bruno, A.; Iqbal, A.; Jamaludin, N. F.; Soci, C.; Mhaisalkar, S.; Mathews, N. Designing Efficient Energy Funneling Kinetics in Ruddlesden-Popper Perovskites for High-Performance Light-Emitting Diodes. *Adv. Mater.* **2018**, *30*, No. 1800818.
- (25) Shi, Y. M.; Hu, J. R.; Chen, J.; Xu, Y. X.; Yang, W. T.; Chen, J. N.; He, Y. B. 5-Ammoniumvaleric acid stabilized mixed-dimensional perovskite submicron platelets with white light emission. *Nanoscale Adv* **2020**, *2*, 4822–4829.
- (26) Kennard, R. M.; Dahlman, C. J.; Chung, J.; Cotts, B. L.; Mikhailovsky, A. A.; Mao, L. L.; DeCrescent, R. A.; Stone, K. H.; Venkatesan, N. R.; Mohtashami, Y.; Assadi, S.; Salleo, A.; Schuller, J. A.; Seshadri, R.; Chabinyc, M. L. Growth-Controlled Broad Emission in Phase-Pure Two-Dimensional Hybrid Perovskite Films. *Chem. Mater.* **2021**, 33, 7290–7300.
- (27) Li, X.; Ke, W.; Traore, B.; Guo, P.; Hadar, I.; Kepenekian, M.; Even, J.; Katan, C.; Stoumpos, C. C.; Schaller, R. D.; Kanatzidis, M. G. Two-Dimensional Dion-Jacobson Hybrid Lead Iodide Perovskites with Aromatic Diammonium Cations. *J. Am. Chem. Soc.* **2019**, *141*, 12880–12890.
- (28) Shi, P. P.; Lu, S. Q.; Song, X. J.; Chen, X. G.; Liao, W. Q.; Li, P. F.; Tang, Y. Y.; Xiong, R. G. Two-Dimensional Organic-Inorganic Perovskite Ferroelectric Semiconductors with Fluorinated Aromatic Spacers. J. Am. Chem. Soc. 2019, 141, 18334–18340.
- (29) Gao, L.; Li, X.; Traore, B.; Zhang, Y.; Fang, J.; Han, Y.; Even, J.; Katan, C.; Zhao, K.; Liu, S.; Kanatzidis, M. G. m-Phenylenediammonium as a New Spacer for Dion-Jacobson Two-Dimensional Perovskites. J. Am. Chem. Soc. 2021, 143, 12063—12073.
- (30) Lemmerer, A.; Billing, D. G. Two packing motifs based upon chains of edge-sharing PbI6 octahedra. *Acta Crystallogr., Sect. C: Cryst. Struct. Commun.* **2006**, *62*, 597–601.
- (31) Mao, L. L.; Stoumpos, C. C.; Kanatzidis, M. G. Two-Dimensional Hybrid Halide Perovskites: Principles and Promises. *J. Am. Chem. Soc.* **2019**, *141*, 1171–1190.
- (32) Vasileiadou, E. S.; Wang, B.; Spanopoulos, I.; Hadar, I.; Navrotsky, A.; Kanatzidis, M. G. Insight on the Stability of Thick Layers in 2D Ruddlesden-Popper and Dion-Jacobson Lead Iodide Perovskites. *J. Am. Chem. Soc.* **2021**, *143*, 2523–2536.
- (33) Marchenko, E. I.; Korolev, V. V.; Mitrofanov, A.; Fateev, S. A.; Goodilin, E. A.; Tarasov, A. B. Layer Shift Factor in Layered Hybrid Perovskites: Univocal Quantitative Descriptor of Composition-Structure-Property Relationships. *Chem. Mater.* **2021**, *33*, 1213–1217.
- (34) Shibuya, K.; Koshimizu, M.; Nishikido, F.; Saito, H.; Kishimoto, S. Poly[bis(phenethyl-ammonium) [di-bromido-plumbate(II)]-di-mu-bromido]]. Acta Crystallogr Sect E Struct Rep Online 2009, 65, 1323–1324.
- (35) Smith, M. D.; Jaffe, A.; Dohner, E. R.; Lindenberg, A. M.; Karunadasa, H. I. Structural origins of broadband emission from layered Pb-Br hybrid perovskites. *Chem. Sci.* **2017**, *8*, 4497–4504.
- (36) Janiak, C. A critical account on pi-pi stacking in metal complexes with aromatic nitrogen-containing ligands. *J. Chem. Soc., Dalton Trans.* **2000**, 3885–3896.
- (37) Lufaso, M. W.; Woodward, P. M. Jahn-Teller distortions, cation ordering and octahedral tilting in perovskites. *Acta Crystallogr., B: Struct. Sci.* **2004**, *60*, 10–20.

- (38) Alonso, J. A.; Martinez-Lope, M. J.; Casais, M. T.; Fernandez-Diaz, M. T. Evolution of the Jahn-Teller distortion of MnO6 octahedra in RMnO3 perovskites (R = Pr, Nd, Dy, Tb, Ho, Er, Y): A neutron diffraction study. *Inorg. Chem.* **2000**, *39*, 917–923.
- (39) Robinson, K.; Gibbs, G. V.; Ribbe, P. H. Quadriatic Elongation Quantitative Measure of Distortion in Coordination Polyhedra. *Science* **1971**, *172*, 567–572.
- (40) Lee, J. H.; Bristowe, N. C.; Bristowe, P. D.; Cheetham, A. K. Role of hydrogen-bonding and its interplay with octahedral tilting in CH3NH3Pb13. *Chem. Commun.* **2015**, *51*, 6434–6437.
- (41) Kubicki, D. J.; Stranks, S. D.; Grey, C. P.; Emsley, L. NMR spectroscopy probes microstructure, dynamics and doping of metal halide perovskites. *Nat Rev Chem* **2021**, *5*, 624–645.
- (42) Spanopoulos, I.; Hadar, I.; Ke, W. J.; Guo, P. J.; Mozur, E. M.; Morgan, E.; Wang, S. X.; Zheng, D.; Padgaonkar, S.; Reddy, G. N. M.; Weiss, E. A.; Hersam, M. C.; Seshadri, R.; Schaller, R. D.; Kanatzidis, M. G. Tunable Broad Light Emission from 3D "Hollow" Bromide Perovskites through Defect Engineering. *J. Am. Chem. Soc.* **2021**, *143*, 7069–7080.
- (43) Kazemi, M. A. A.; Raval, P.; Cherednichekno, K.; Chotard, J. N.; Krishna, A.; Demortiere, A.; Reddy, G. N. M.; Sauvage, F. Molecular-Level Insight into Correlation between Surface Defects and Stability of Methylammonium Lead Halide Perovskite Under Controlled Humidity. *Small Methods* **2021**, *5*, No. 2000834.
- (44) Krishna, A.; Zhang, H.; Zhou, Z. W.; Gallet, T.; Dankl, M.; Ouellette, O.; Eickemeyer, F. T.; Fu, F.; Sanchez, S.; Mensi, M.; Zakeeruddin, S. M.; Rothlisberger, U.; Reddy, G. N. M.; Redinger, A.; Gratzel, M.; Hagfeldt, A. Nanoscale interfacial engineering enables highly stable and efficient perovskite photovoltaics. *Energy Environ. Sci.* 2021, 14, 5552–5562.
- (45) Dahlman, C. J.; Kennard, R. M.; Paluch, P.; Venkatesan, N. R.; Chabinyc, M. L.; Reddy, G. N. M. Dynamic Motion of Organic Spacer Cations in Ruddlesden-Popper Lead Iodide Perovskites Probed by Solid-State NMR Spectroscopy. *Chem. Mater.* **2021**, 33, 642–656.
- (46) Piveteau, L.; Morad, V.; Kovalenko, M. V. Solid-State NMR and NQR Spectroscopy of Lead-Halide Perovskite Materials. *J. Am. Chem. Soc.* **2020**, *142*, 19413–19437.
- (47) Raval, P.; Kennard, R. M.; Vasileiadou, E. S.; Dahlman, C. J.; Spanopoulos, I.; Chabinyc, M. L.; Kanatzidis, M.; Reddy, G. N. M. Understanding Instability in Formamidinium Lead Halide Perovskites: Kinetics of Transformative Reactions at Grain and Subgrain Boundaries br. ACS Energy Lett. 2022, 7, 1534–1543.
- (48) Stoumpos, C. C.; Kanatzidis, M. G. The Renaissance of Halide Perovskites and Their Evolution as Emerging Semiconductors. *Acc. Chem. Res.* **2015**, *48*, 2791–2802.
- (49) Stoumpos, C. C.; Mao, L. L.; Malliakas, C. D.; Kanatzidis, M. G. Structure-Band Gap Relationships in Hexagonal Polytypes and Low-Dimensional Structures of Hybrid Tin Iodide Perovskites. *Inorg. Chem.* **2017**, *56*, 56–73.
- (50) Wang, N. N.; Cheng, L.; Ge, R.; Zhang, S. T.; Miao, Y. F.; Zou, W.; Yi, C.; Sun, Y.; Cao, Y.; Yang, R.; Wei, Y. Q.; Guo, Q.; Ke, Y.; Yu, M. T.; Jin, Y. Z.; Liu, Y.; Ding, Q. Q.; Di, D. W.; Yang, L.; Xing, G. C.; Tian, H.; Jin, C. H.; Gao, F.; Friend, R. H.; Wang, J. P.; Huang, W. Perovskite light-emitting diodes based on solution-processed self-organized multiple quantum wells. *Nat. Photonics* **2016**, *10*, 699–705.
- (S1) Gao, L. L.; Li, X. T.; Traore, B.; Zhang, Y. L.; Fang, J.; Han, Y.; Even, J.; Katan, C.; Zhao, K.; Liu, S. Z.; Kanatzidis, M. G. m-Phenylenediammonium as a New Spacer for Dion-Jacobson Two-Dimensional Perovskites. *J. Am. Chem. Soc.* **2021**, *143*, 12063–12073.
- (52) Dhanabalan, B.; Castelli, A.; Palei, M.; Spirito, D.; Manna, L.; Krahne, R.; Arciniegas, M. Simple fabrication of layered halide perovskite platelets and enhanced photoluminescence from mechanically exfoliated flakes. *Nanoscale* **2019**, *11*, 8334–8342.
- (53) Ma, Z.; Li, F.; Sui, L.; Shi, Y.; Fu, R.; Yuan, K.; Xiao, G.; Zou, B. Tunable Color Temperatures and Emission Enhancement in 1D Halide Perovskites under High Pressure. *Adv. Opt. Mater.* **2020**, 8, No. 2000713.

- (54) Cortecchia, D.; Yin, J.; Petrozza, A.; Soci, C. White light emission in low-dimensional perovskites. *Journal of Materials Chemistry C* **2019**, 7, 4956–4969.
- (55) Febriansyah, B.; Borzda, T.; Cortecchia, D.; Neutzner, S.; Folpini, G.; Koh, T. M.; Li, Y.; Mathews, N.; Petrozza, A.; England, J. Metal Coordination Sphere Deformation Induced Highly Stokes-Shifted, Ultra Broadband Emission in 2D Hybrid Lead-Bromide Perovskites and Investigation of Its Origin. *Angew. Chem., Int. Ed.* **2020**, *59*, 10791–10796.
- (56) Smith, M. D.; Connor, B. A.; Karunadasa, H. I. Tuning the Luminescence of Layered Halide Perovskites. *Chem. Rev.* **2019**, *119*, 3104–3139.
- (57) Sham, L. J.; Schlüter, M. Density-Functional Theory of the Energy Gap. *Phys. Rev. Lett.* **1983**, *51*, 1888–1890.
- (58) Bala, A.; Deb, A. K.; Kumar, V. Atomic and Electronic Structure of Two-Dimensional Inorganic Halide Perovskites A(n+1)M(n)X(3n+1) (n=1-6, A = Cs, M = Pb and Sn, and X = Cl, Br, and I) from ab Initio Calculations. *J. Phys. Chem. C* **2018**, 122, 7464–7473.
- (59) Mao, L. L.; Kennard, R. M.; Traore, B.; Ke, W. J.; Katan, C.; Even, J.; Chabinyc, M. L.; Stoumpos, C. C.; Kanatzidis, M. G. Seven-Layered 2D Hybrid Lead Iodide Perovskites. *Chem* **2019**, *5*, 2593–2604.
- (60) Mao, L. L.; Guo, P. J.; Kepenekian, M.; Spanopoulos, I.; He, Y. H.; Katan, C.; Even, J.; Schaller, R. D.; Seshadri, R.; Stoumpos, C. C.; Kanatzidis, M. G. Organic Cation Alloying on Intralayer A and Interlayer A' sites in 2D Hybrid Dion-Jacobson Lead Bromide Perovskites (A')(A)Pb2B7. J. Am. Chem. Soc. 2020, 142, 8342–8351.
- (61) Hadi, A.; Ryan, B. J.; Nelson, R. D.; Santra, K.; Lin, F. Y.; Cochran, E. W.; Panthani, M. G. Improving the Stability and Monodispersity of Layered Cesium Lead Iodide Perovskite Thin Films by Tuning Crystallization Dynamics. *Chem. Mater.* **2019**, *31*, 4990–4998.
- (62) Sidhik, S.; Li, W. B.; Samani, M. H. K.; Zhang, H.; Wang, Y. F.; Hoffman, J.; Fehr, A. K.; Wong, M. S.; Katan, C.; Even, J.; Marciel, A. B.; Kanatzidis, M. G.; Blancon, J. C.; Mohite, A. D. Memory Seeds Enable High Structural Phase Purity in 2D Perovskite Films for High-Efficiency Devices. *Adv. Mater.* **2021**, *33*, No. 2007176.
- (63) Reddy, G. N. M.; Malon, M.; Marsh, A.; Nishiyama, Y.; Brown, S. P. Fast Magic-Angle Spinning Three-Dimensional NMR Experiment for Simultaneously Probing H-H and N-H Proximities in Solids. *Anal. Chem.* **2016**, *88*, 11412–11419.

☐ Recommended by ACS

Effect of Dimensionality on Photoluminescence and Dielectric Properties of Imidazolium Lead Bromides

Szymon Smółka, Maciej Ptak, et al.

SEPTEMBER 14, 2022 INORGANIC CHEMISTRY

READ 🗹

Thick-Layer Lead Iodide Perovskites with Bifunctional Organic Spacers Allylammonium and Iodopropylammonium Exhibiting Trap-State Emission

Eugenia S. Vasileiadou, Mercouri G. Kanatzidis, et al.

APRIL 05, 2022

JOURNAL OF THE AMERICAN CHEMICAL SOCIETY

READ 🗹

Band Edge Engineering of 2D Perovskite Structures through Spacer Cation Engineering for Solar Cell Applications

Eti Mahal, Biswarup Pathak, et al.

JUNE 07, 2022

THE JOURNAL OF PHYSICAL CHEMISTRY C

RFAD **「**へ

Two-Dimensional Organic-Inorganic Hybrid Materials with Dielectric Switching and Photoluminescence Properties

Qiang-Qiang Jia, Hai-Feng Lu, et al.

APRIL 06, 2022

CRYSTAL GROWTH & DESIGN

READ 🗹

Get More Suggestions >